PCCP

Accepted Manuscript

ROYAL SOCIETY OF CHEMISTRY

www.rsc.org/pccp

CREATED USING THE RSC LaTeX PCCP ARTICLE TEMPLATE – SEE www.rsc.org/electronicfiles FOR DETAILS

ARTICLE TYPE www. rsc.org/xxxxxx | XXXXXXXX

Where does the Raman optical activity of $[Rh(en)_3]^{3+}$ come from? Insight from a combined experimental and theoretical approach†

Marie Humbert-Droz,[a] Patric Oulevey,*[a] Latévi Max Lawson Daku,[a] Sandra Luber,[b] Hans Hagemann,[a] and Thomas Bürgi[a]

Received Xth XXXXXXXXXX 20XX, Accepted Xth XXXXXXXXX 20XX

First published on the web Xth XXXXXXXXXX 200X

DOI: 10.1039/b000000x

Backscattered Raman optical activity (ROA) spectra are measured for Δ- and Λ-*tris*-(ethylenediamine)rhodium(III) chloride in aqueous solution. In addition, the spectra of the four possible conformers in the Λ configuration are investigated by *ab-initio* calculations. The Λ($\delta\delta\delta$) conformer is in best agreement with experimental spectra and examined in more details. The two most stable conformers according to the calculations are not compatible with the experimental ROA spectrum. Insights into the origin of observed band intensities are obtained by means of group coupling matrices. The influence of the first solvation shell is explored via an *ab-initio* molecular dynamics simulation. Taking explicit solvent molecules into account further improves the agreement between calculation and experiment. Analysis of selected normal modes using group coupling matrices shows that solvent molecules lead to normal mode rotation and thus contribute to the ROA intensity, whereas the contribution of the Rh can be neglected.

† Electronic Supplementary Information (ESI) available: [details of any supplementary information available should be included here]. See DOI: 10.1039/b000000x/

[a] *University of Geneva, Department of Physical Chemistry, Quai Ernest-Ansermet 30, CH-1211 Geneva 4, Switzerland. Fax: +41 22 3796103; Tel: +41 22 3796556; E-mail: patric.oulevey@unige.ch*

[b] *University of Zurich, Department of Chemistry, Winterthurerstrasse 190, CH-8057 Zurich, Switzerland.*

1 Introduction

Spectroscopic techniques exploiting the natural vibrational optical activity (VOA) of chiral molecules have proven remarkably useful. Generally VOA refers to the fact that for asymmetric molecules the interaction with left and right circularly polarized light is slightly different; vibrational experimental techniques enclosed by VOA are called vibrational circular dichroism (VCD) and Raman optical activity (ROA) which represent particular forms of IR absorption and Raman scattering spectroscopies, respectively. An elaborate comparison of VCD and ROA has been published by Nafie *et al.* [1] For recent review articles covering theoretical and experimental aspects of VOA we refer to references 2–4. The focus is exclusively set on ROA in the presented study and therefore the discussion is limited to that part of VOA.

Since the differential intensity of the two circular components of the light is very small, the construction of ROA spectrometers able to capture both components with high enough precision was utterly challenging and could be achieved in the early 1970's [5–8]. A leap in instrumentation, once by employing new polarization schemes [9], and due to improved detectors and design, was accomplished about 20 years later [10,11]. With these instruments structural insight has been gained into a wide range of molecular systems: they can record difference spectra of small molecules, e.g., chirally deuterated neopentane [12], or give valuable information about conformations in polypeptides [13] and the tertiary structures of proteins. [14,15] Recently ROA was used for *in situ* analysis of human blood plasma and other biofluids [16]. With respect to transition metal complexes, only a few studies have been published [17–20]; the opposite is the case, however, for VCD investigations of such compounds, see, e.g., references 21–24.

In this paper, we report the vibrational ROA characterization of a chiral transition metal complex, *tris*(ethylenediamine)rhodium(III), $[Rh(en)_3]^{3+}$, in aqueous solution. This d^6 complex presents the advantage that near-resonance problems are avoided since it does not absorb in the vicinity of 532 nm, which is the laser wavelength used for the ROA measurements and is, besides the (*S*,*S*)-en(thind)$_2$ZrCl$_2$ complex reported by Johannessen *et al.* [18], one of first complexes for whose (off-resonant) experimental ROA spectra are now available. The study combines the measurement of Raman and ROA spectra and their analyses based on quantum chemical calculations. Because the solute-solvent interactions are likely to significantly influence the recorded spectra [25,26], solvents effects were included in the calculations. In a first approach, an implicit solvation model was used. A vibrational analysis based upon these calculations was done and, for selected spectral bands, the origin of band intensities was further investigated by means of group-coupling matrices (GCMs). Thereafter, in order to probe the influence of the specific solute-solvent interactions on the spectra, explicit water molecules were added guided by the results of an *ab initio* molecular dynamics (AIMD) simulation.

The discriminatory power of VOA spectroscopies, not only for configurations but equally for conformations, makes these methods ideal to investigate chiral compounds. *Tris*(ethylenediamine) complexes exist in two enantiomeric forms and a limited number of four different conformations per enantiomer. To denote the different forms (configurations) and conformations, we utilize the skew-line convention for *tris*(bidentate) complexes recommended by IUPAC, paragraph IR-9.3.4.11 in reference 27. In summary, the configurations, reflecting the two possibilities to arrange bidentate ligands in an octahedral structure, are labeled *delta* (Δ) and *lambda* (Λ). In addition to that, each ligand can adopt either δ or λ conformation also determined by two skew-lines. Combining the configuration and conformation, one should consider a total of eight different structures: $\Lambda(\delta\delta\delta)$, $\Lambda(\delta\delta\lambda)$, $\Lambda(\delta\lambda\lambda)$, $\Lambda(\lambda\lambda\lambda)$, $\Delta(\lambda\lambda\lambda)$, $\Delta(\lambda\delta\delta)$, $\Delta(\lambda\lambda\delta)$, and $\Delta(\delta\delta\delta)$. Because of the mirror image relationship between the Λ and Δ configurations, the calculations were only performed on the four conformers (all λ/δ combinations) of the Λ configuration. Figure 1 shows these four considered structures.

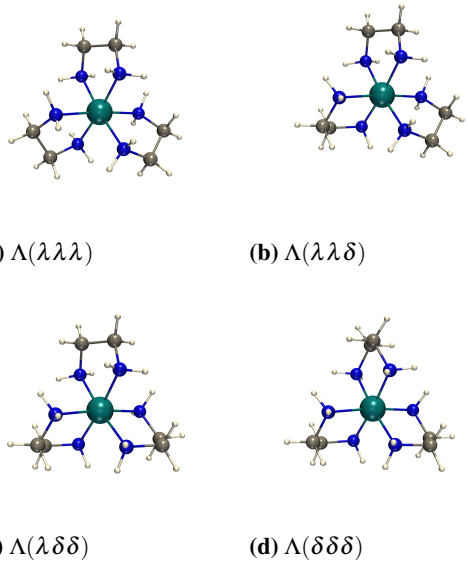

(a) $\Lambda(\lambda\lambda\lambda)$ **(b)** $\Lambda(\lambda\lambda\delta)$

(c) $\Lambda(\lambda\delta\delta)$ **(d)** $\Lambda(\delta\delta\delta)$

Fig. 1 Possible conformations for the Λ configuration of *tris*(ethylenediamine)-rhodium(III). The ligands can either adopt the λ or δ conformation

2 Experimental and Computational Details

2.1 Synthesis

Δ- and Λ-*tris*(ethylenediamine)-rhodium(III) chloride hydrate, $[Rh(en)_3]Cl_3 \cdot 3\,H_2O$, have been prepared according to the procedure described by Galsbøl[28]. For the enantioseparation the fact was exploited that $\Lambda-[Rh(en)_3]^{3+}$ forms a double salt with the $(+)$-tartrate anion and precipitates upon addition of this anion and $Li(OH) \cdot H_2O$ in aqueous solution, while $\Delta-[Rh(en)_3]Cl_3 \cdot 3\,H_2O$ remains dissolved. The former $[Rh(en)_3]^{3+}$ containing double salt can be purified and converted to the chloride, while the latter form of the complex is extracted from the solution by addition of HCl and ethanol. More information can be found in the supporting information (SI).

2.2 Raman and ROA Measurements

The spectra of Δ- and Λ-$[Rh(en)_3]^{3+}$ have each been obtained from three individual acquisitions (totally 41 minutes) with a laser power of 300 mW at the sample. A custom made quartz cell[29] providing a sample volume of 35 μl has been used to contain the solutions with a concentration of 0.625 M in water.

The spectra have been recorded using the scattered circular polarization (SCP) scheme[29] in back scattering geometry with the spectrometer constructed by Hug and coworkers[12,30]. The instrument was carefully designed for offset reduction[11,31].

2.3 Computational Details

The computational characterization of $[Rh(en)_3]^{3+}$ has been done within the Kohn-Sham formulation of density functional theory (DFT).[32,33] The calculations were performed with the B3LYP hybrid exchange-correlation functional[34–36] because of its good performance for ROA calculations[25,26,37–40]. In order to have a good description of the dispersion interactions, we employed the D2 dispersion correction of Grimme. The influence of the water solvent was taken into account through the use of the integral equation formalism of the polarizable continuum model (IEFPCM)[41]. The calculations were performed with the Gaussian 09 Revision C.01 program package[42]. The ROA intensities were computed analytically[43–46] using the same theoretical level as the one used for the geometry optimization. To assess the influence of the basis set, the ROA spectrum of the $\Lambda(\lambda\lambda\lambda)$ conformer has been calculated using three different Gaussian basis sets. In the first basis set, the H, N, and C atoms are described by the TZVP basis set of valence triple-ζ polarized quality[47], while the core of the Rh atom is modeled by a relativistic compact effective potential (CEP) and its valence electrons are described by the CEP-121 triple-ζ polarized basis set[48]. In the second and larger basis set, all atoms are described by the def2-TZVP basis set of valence triple-ζ polarized quality[49]. For Rh, the basis set was used with the accompanying effective core potential (ECP-28)[50]. The third and largest basis set

consists in the augmented def2-TZVPD basis set, which has been designed for molecular response calculations and which is obtained from the def2-TZVP basis set by the addition of a small number of moderately diffuse basis functions[51]. For Rh, use of the same ECP-28 was made. The basis set dependence study showed that the calculated spectrum does no more evolve beyond the use of the def2-TZVP basis set, which was thus retained for the characterization of all conformers. In the Gaussian 09 revision used, notably C.01, the Hamiltonian is not gauge invariant when ECPs are used and this might result in erroneous results[52]. To check the quality of the performed calculations, the values of the G tensor and the β_G^2 ROA invariant, that is related to this tensor, obtained with Gaussian 09 revisions C.01 and D.01 (in the latter the issue of gauge invariance has been accounted for) have been compared for the $\Lambda(\lambda\lambda\delta)$ conformer. Only very small and uncritical deviations could be observed; the spectra for these test calculations are given in the as Supporting Information (SI).

A series of spectra showing the influence of the implicit solvent model and of the basis sets are available as Supporting Information (SI).

The structure of the $\Lambda(\delta\delta\delta)$ conformer of $[Rh(en)_3]^{3+}$ in aqueous solution and the organization of its solvation shell have been characterized by Born-Oppenheimer molecular dynamics (BOMD) simulation performed at 300 K. A large cubic box with a side length of 16 Å containing a $\Lambda(\delta\delta\delta)$ conformer and 121 water molecules was used. It has been generated using utilities from the GROMACS program package[53] and an equilibrated water box[54]. The simulation was performed with the PBE functional augmented with the semi-empirical dispersion correction of Grimme (PBE-D3)[55] and the hybrid Gaussian and planewave (GPW) method as implemented in the CP2K/QUICKSTEP program[56]. The core electrons of the atoms were described with Goedecker-Teter-Hutter pseudopotentials[57–59], while their valence states were described with the Gaussian-type MOLOPT[60] DZVP-MOLOPT-SR-GTH basis set of double-zeta polarized quality from the CP2K package. The electron density was expanded in a planewave basis set using a planewave cutoff of 280 Ry and a relative density cutoff of 40 Ry was used. A 0.5 fs timestep was employed in the integration of the equations of motion. The system was equilibrated for 2.90 ps at constant temperature using the Nosé-Hoover thermostat chain[61]. Thermostating was kept on during the production run of 33.86 ps during which the trajectory was recorded every 10 steps. The analysis of the recorded trajectory was carried out using the GROMACS utilities. The VMD[62,63] and Jmol[64,65] programs were used for visualization of the MD results.

The PyVib2[66] program was used to treat experimental and theoretical spectroscopic data. For the representation of the latter a band profile obtained from 6 Gaussian functions was used; the values for the full width at half maximum (FWHM) for isotropic and anisotropic contributions were set to 12 cm^{-1} and 15 cm^{-1}, respectively.

3 Results and Discussion

Figure 2 shows the experimental spectra of the two enantiomers of $[Rh(en)_3]^{3+}$. Identifiers (ν_1–ν_{13}) were added over some bands for easy referencing in further analysis. Table 1 gives the description of the atomic displacements of these bands, based on the computational results. Before proceeding to the detailed analysis of the experimental spectra, we give a brief overview of the theory of ROA calculations.

3.1 Theoretical Background

The foundation of the theoretical prediction of Raman scattering of chiral molecules has been set around 1970[67,68]; general expressions for the different scattering polarization schemes followed in the early 1990's[69]. The following formulae are given for the SCP scheme, naturally polarized incident light, and backward scattering ($\theta = 180°$). For other polarization schemes and scattering directions the reader is referred to ref. 69, chapter 7.3 in ref. 70, ref. 71, and chapter 5 in ref. 4.

For isotropically oriented molecules (with a statistical distribution of their spatial orientation) in the scattering zone in the far from resonance limit

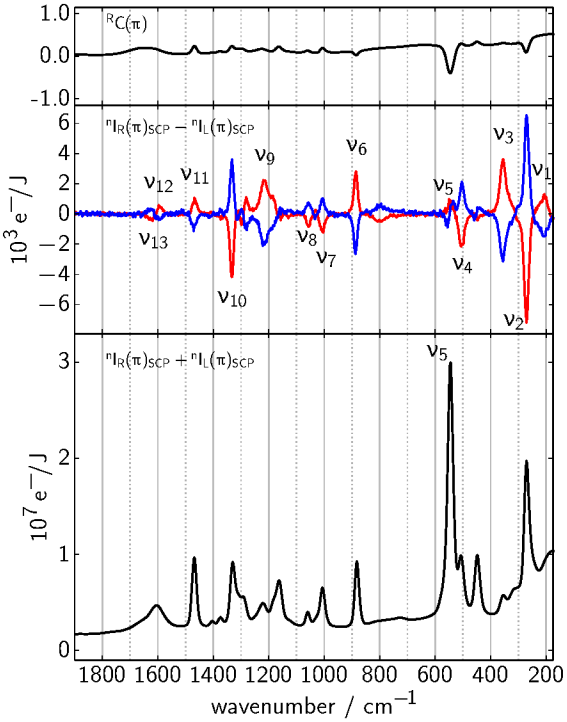

Fig. 2 Experimental backscattering Raman, ROA, and degree of circularity spectra of Λ-$[Rh(en)_3]^{3+}$ (red) and Δ-$[Rh(en)_3]^{3+}$ (blue). The Raman and degree of circularity spectra are shown for the Λ configuration only (black). Laser wavelength : 532 nm. Labeled bands will further be discussed

Table 1 Description of selected vibrational bands of $[Rh(en)_3]^{3+}$ based on computational results of the $\Lambda(\delta\delta\delta)$ conformer (B3LYP-D2/def2-TZVP, IEFPCM)

vib.	cm^{-1}	Description of vibration
ν_1	203	en deformation
ν_2	269	en breathing
ν_3	355	N−C−C−N torsion
ν_4	502	*out-of-phase* en scissoring
ν_5	546	*in-phase* en scissoring
ν_6	884	C−C and C−N stretching, CH_2 rocking
ν_7	1005	CH_2 rocking, NH_2 twisting
ν_8	1057	C−C stretching
ν_9	1215	NH_2 wagging
ν_{10}	1332	NH_2 wagging, CH_2 twisting
ν_{11}	1466	CH_2 scissoring
ν_{12}	1598	NH_2 scissoring
ν_{13}	1617	NH_2 scissoring

the molecular quantities for the differential Raman and ROA scattering cross sections per unit solid angle Ω are given by combinations of invariants I ($I = \{a^2, \beta^2, \beta_G^2, \beta_A^2\}$):

$$^{n}d\sigma(180^\circ)_{SCP} = K\left(90a^2 + 14\beta^2\right)d\Omega, \quad (1)$$

$$-\Delta^{n}d\sigma(180^\circ)_{SCP} = \frac{4K}{c}\left(12\beta_G^2 + 4\beta_A^2\right)d\Omega \quad (2)$$

where K stands for the factor

$$K = K_p = \frac{1}{90}\left(\frac{\mu_0}{4\pi}\right)^2 \omega_0 \omega_p^3 \quad (3)$$

for a vibration p. ω_0 and ω_p are the pulsations of the incident and scattered light, respectively. The formulae in this subsection are reproduced from reference 72, to some extent rearranged, but the notation is conserved (with the exception for an invariant, which is denoted I in this paper). For detailed insight we refer to the previously cited works. A molecular invariant is expressed as sum of mono- ($a = b$) and di-nuclear ($a \neq b$) reduced invariant

terms J_{ab},

$$a^2_{ab,p} = \tfrac{1}{3}\,\underline{\underline{\alpha}}^{is}_{a,p} : \underline{\underline{\alpha}}^{is}_{b,p} \approx F_p\, J(a^2)_{ab,p}, \quad (4)$$

$$\beta^2_{ab,p} = \tfrac{3}{2}\,\underline{\underline{\alpha}}^{anis}_{a,p} : \underline{\underline{\alpha}}^{anis}_{b,p} \approx F_p\, J(\beta^2)_{ab,p}, \quad (5)$$

$$\beta^2_{Gab,p} = \tfrac{3}{2}\,\underline{\underline{\alpha}}^{anis}_{a,p} : \underline{\underline{G'}}_{b,p} \approx F_p\, J(\beta^2_G)_{ab,p}, \quad (6)$$

$$\beta^2_{Aab,p} = \tfrac{\omega_0}{2}\,\underline{\underline{\alpha}}^{anis}_{a,p} : \underline{\underline{\mathscr{A}}}_{b,p} \approx F_p\, J(\beta^2_A)_{ab,p} \quad (7)$$

with $F_p = \hbar\,(400\pi c \Delta\tilde{\nu}_p)^{-1}$. The number of underscores denotes the rank of the tensor, and $\Delta\tilde{\nu}_p$ corresponds to the Raman frequency shift in cm^{-1}. The real electronic property tensors[72,73] $\underline{\underline{\alpha}}$, $\underline{\underline{G'}}$, and $\underline{\underline{\underline{A}}}$ have been obtained with Gaussian 09[42]. These three tensors contain the elements of the electric dipole-electric dipole, the imaginary part of the electric dipole-magnetic dipole, and electric dipole-electric quadrupole interactions, respectively. $\underline{\underline{\mathscr{A}}}$ is obtained from $\underline{\underline{\underline{A}}}$ with use of the totally antisymmetric Levi-Civita unit tensor $\underline{\underline{\underline{\varepsilon}}}$, $\mathscr{A}_{\mu\nu} = \sum_{\rho\sigma} \varepsilon_{\mu\rho\sigma} A_{\rho,\sigma\nu}$.

The reduced invariants $J_{ab,p}$ for a vibration p, and the atoms a and b are composed of normalized Cartesian displacement vectors ($L^x_{a,p}$ and $L^x_{b,p}$) and electronic V tensors ($\underline{\underline{V}}_{ab}$),

$$J(I)_{ab,p} = \underline{L}^x_{a,p} \cdot \underline{\underline{V}}(I)_{ab} \cdot \underline{L}^x_{b,p} \quad (8)$$

where I stands for the invariant of interest. The elements of the V tensors for the five invariants of used for Raman and ROA backscattering spectra are given by the expressions

$$V(a^2)_{ai,bj} = \frac{1}{9}\sum_{\mu\nu}\left(\frac{\partial\alpha_{\mu\mu}}{\partial x^a_i}\right)_0\left(\frac{\partial\alpha_{\nu\nu}}{\partial x^b_j}\right)_0, \quad (9)$$

$$V(\beta^2)_{ai,bj} = \frac{1}{2}\sum_{\mu\nu}\left\{3\left(\frac{\partial\alpha_{\mu\nu}}{\partial x^a_i}\right)_0\left(\frac{\partial\alpha_{\mu\nu}}{\partial x^b_j}\right)_0 - \left(\frac{\partial\alpha_{\mu\mu}}{\partial x^a_i}\right)_0\left(\frac{\partial\alpha_{\nu\nu}}{\partial x^b_j}\right)_0\right\}, \quad (10)$$

$$V(\beta^2_G)_{ai,bj} = \frac{1}{2}\sum_{\mu\nu}\left\{3\left(\frac{\partial\alpha_{\mu\nu}}{\partial x^a_i}\right)_0\left(\frac{\partial G'_{\mu\nu}}{\partial x^b_j}\right)_0 - \left(\frac{\partial\alpha_{\mu\mu}}{\partial x^a_i}\right)_0\left(\frac{\partial G'_{\nu\nu}}{\partial x^b_j}\right)_0\right\}, \quad (11)$$

$$V(\beta^2_A)_{ai,bj} = \frac{\omega_0}{2}\sum_{\mu\nu}\left(\frac{\partial\alpha_{\mu\nu}}{\partial x^a_i}\right)_0\left(\frac{\partial\mathscr{A}_{\mu\nu}}{\partial x^b_j}\right)_0 \quad (12)$$

where i and j define the component of the nuclear position vector ($\underline{x}$) and the summation is carried out over tensor elements indexed by μ and ν. The subscript 0 after brackets indicates that the system was taken at its equilibrium geometry. For further analysis it is desirable to split the terms of reduced invariants depending on the selected atoms a and b to distinct fragments of the molecule. Atoms in a molecule can be assigned to groups (A, B, C...) and due to the additivity of the parts of reduced invariants defined in equation 8, J can be separated into contributions of groups as follows

$$J = J(A)_p + J(B)_p + \ldots \quad (13)$$

$$.. + J(A,B)_p + \quad J(B,C)_p + \ldots, \quad (14)$$

$$J(A)_p = \sum_{a,b} J_{ab,p}, \qquad a,b \in A, \quad (15)$$

$$J(A,B)_p = \sum_{a,b}\left(J_{ab,p} + J_{ba,p}\right), \qquad a \in A, b \in B \quad (16)$$

So-called *group coupling matrices* (GCMs) can be formed which represent the resulting intra-group (mono- and di-nuclear) and inter-group (only di-nuclear) terms. The elements are represented in an upper triangular matrix. This allows, in the context of this work, to define for example individual groups for the three ethylenediamine (en) ligands

and the rhodium atom for the construction of GCMs (see later).

The Cartesian displacement vectors used in formula 8, the V tensors in formulae 9–12, and the group coupling matrices have been obtained with a development version of PyVib2[66] employing the data mentioned earlier calculated by Gaussian 09.

3.2 Vibrational Analysis

The values found for selected structural parameters in the optimized geometries of the conformers of $[Rh(en)_3]^{3+}$ are summarized in Table 2. Figure 3 compares experimental (e) and calculated (a–d) ROA and Raman spectra. The sensitivity of ROA spectra to conformational changes are evidently visible in the calculated spectra. Raman spectra show smaller differences.

We will now analyze prominent bands of the ROA spectra in more detail in order to identify the conformer giving the major contribution to the experimental spectrum. The first vibration to be examined here is the band ν_2 in Table 1, attributed to the ligand breathing mode at 269 cm^{-1}. This band is present and strongly negative in all four conformers, reproducing very well the experiment. Bands ν_4 and ν_5 at 502 cm^{-1} and 546 cm^{-1}, respectively, can be attributed to the *out-of-phase* and *in-phase* ethylenediamine scissoring, respectively. For the *out-of-phase* scissoring the experiment shows a strong negative ROA band. We find this pattern in calculated spectra of $\Lambda(\delta\delta\delta)$ and $\Lambda(\lambda\delta\delta)$ conformers. Although the signal is negative for the two other conformers, the intensity is much weaker. Regarding the *in-phase* scissoring, the ROA band is clearly positive in the experiment, as for all calculated conformers. The interesting aspect is the size of these two bands in the Raman and ROA spectra. While the *in-phase* scissoring vibration generates a Raman band with very high intensity and a ROA band with low intensity, the opposite is true for the *out-of-phase* scissoring. This combination is found well reproduced in two conformers, namely $\Lambda(\delta\delta\delta)$ and $\Lambda(\lambda\delta\delta)$. The sequence of a weak followed by a strong Raman band is also predicted for the two other conformers, but as discussed previ-

Table 2 Selected structural parameters obtained in the calculations within the IEFPCM model (B3LYP-D2/def2-TZVP) of the four conformations in the Λ configuration. Bond lengths are given in Å and angles in degrees. The identifiers (*id*) refer to d_1: Rh−N, d_2: Rh−N', β: N−Rh−N', γ: N−C−C'-N'. Values are given for all three ethylenediamine (en) ligands. Experimental values are (for the $\Lambda(\delta\delta\delta)$ conformer) d_1: 2.067, d_2: 2.056, β: 83.6, γ: 55.8[74]

	id	en_1	en_2	en_3
		λ	λ	λ
	d_1	2.104	2.103	2.103
$\Lambda(\lambda\lambda\lambda)$	d_2	2.106	2.107	2.108
	β	82.2	82.2	82.21
	γ	-53.3	-53.4	-52.7
		λ	λ	δ
	d_1	2.104	2.106	2.106
$\Lambda(\lambda\lambda\delta)$	d_2	2.106	2.104	2.106
	β	82.2	82.2	82.2
	γ	-53.4	-53.4	53.1
		λ	δ	δ
	d_1	2.108	2.104	2.102
$\Lambda(\lambda\delta\delta)$	d_2	2.108	2.102	2.104
	β	82.0	82.4	82.4
	γ	-55.5	53.6	53.6
		δ	δ	δ
	d_1	2.104	2.106	2.102
$\Lambda(\delta\delta\delta)$	d_2	2.106	2.104	2.102
	β	82.6	82.6	82.6
	γ	54.4	53.4	52.9

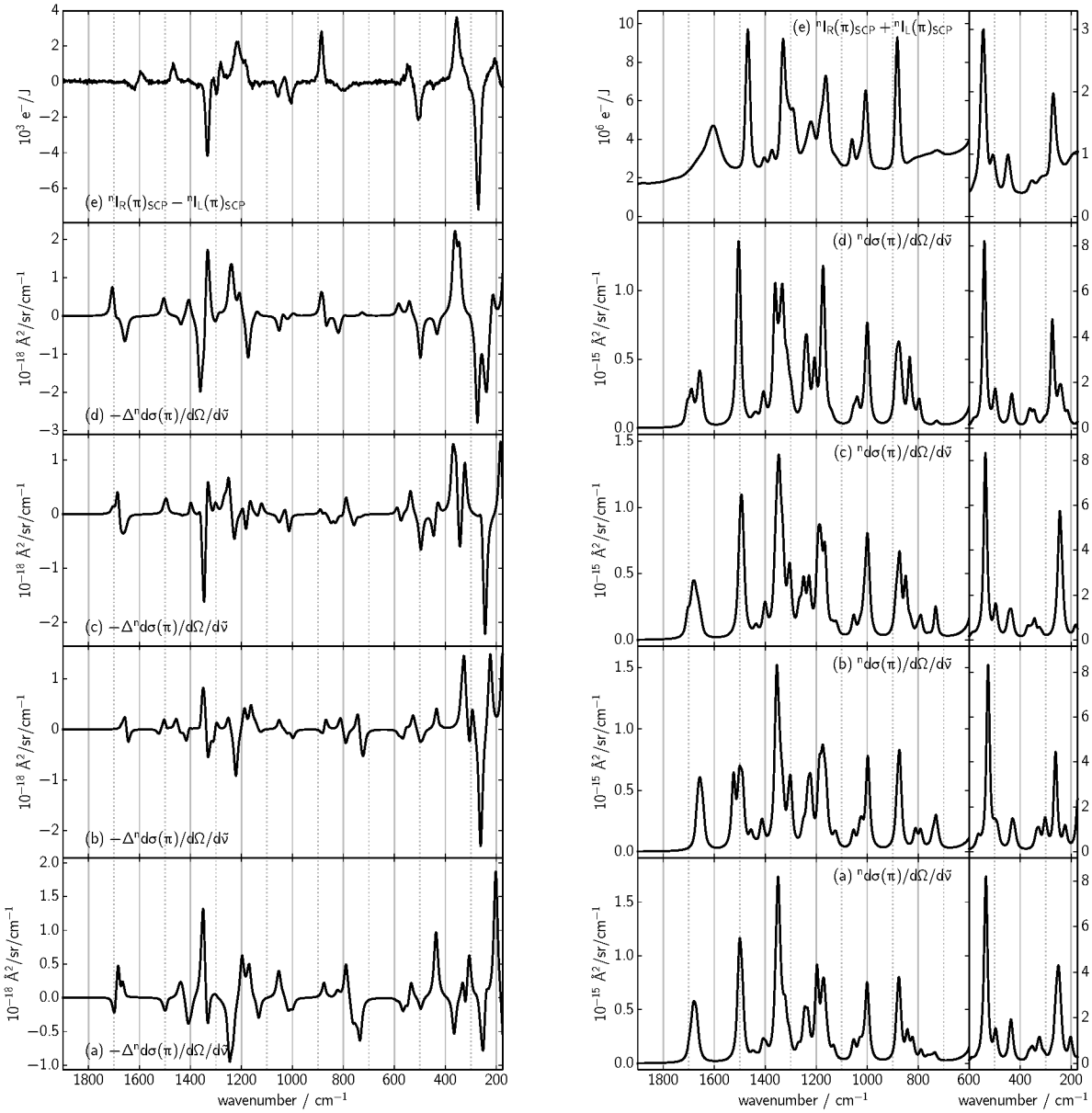

Fig. 3 ROA (*left*) and Raman (*right*) spectra of Λ-*tris*(ethylenediamine)rhodium(III). $\Lambda(\lambda\lambda\lambda)$ conformer (a), $\Lambda(\lambda\lambda\delta)$ conformer (b), $\Lambda(\lambda\delta\delta)$ conformer (c), $\Lambda(\delta\delta\delta)$ conformer (d), and the experimental data (e). Level of theory for the calculated data: B3LYP-D2/def2-TZVP, IEFPCM

ously, the corresponding ROA signals do not match the experiment. Band ν_6 at 884 cm^{-1} represents vibrations comprising C−C and C−N stretching, as well as CH_2 rocking. The signal is strongly positive in the experiment. The calculated spectrum of $\Lambda(\delta\delta\delta)$ shows also a moderately strong positive signal. The agreement between experiment and theory is not good for the three other conformers.

Band ν_7 (1005 cm^{-1}) arises from CH_2 rocking and NH_2 twisting. In the experiment, the band is negative and is well reproduced, in terms of sign and intensity, only by conformer $\Lambda(\lambda\delta\delta)$. The C−C stretching band, represented by band ν_8 (1057 cm^{-1}), is well reproduced by the $\Lambda(\delta\delta\delta)$ and present for the $\Lambda(\lambda\delta\delta)$ conformers in terms of sign and intensity. The two other conformers have opposite sign for this vibration.

Going to band ν_9 at 1215 cm^{-1}, the NH_2 wagging vibration, we can see that the pattern is well reproduced by the $\Lambda(\delta\delta\delta)$ conformer. The corresponding band shows also the shoulder observed in the experiment.

Band ν_{10} (1332 cm^{-1}), representing the NH_2 wagging and CH_2 twisting, is also well reproduced by the $\Lambda(\lambda\delta\delta)$ conformer in terms of intensity and sign. Conformer $\Lambda(\delta\delta\delta)$ shows a strong negative band for this vibration as well, but the positive signal (not observed to that extent in the experiment) at slightly lower Raman shift is stronger. For the two other conformers, the signal has opposite sign. Band ν_{11} (1466 cm^{-1}) is, like most of the bands described previously, well reproduced by conformers $\Lambda(\delta\delta\delta)$ and $\Lambda(\lambda\delta\delta)$. The vibration responsible for this signal is characterized as CH_2 scissoring. The $\Lambda(\lambda\lambda\delta)$ conformer has very weak intensity of this signal compared to the experiment, and shows some negative component. The fourth conformer has a negative signal.

Finally, the last two bands attributed to NH_2 scissoring, ν_{12} and ν_{13} (1598 cm^{-1} and 1617 cm^{-1}), are poorly reproduced by the present calculations. The signs are reversed and therefore the pattern is different (especially for the $\Lambda(\lambda\lambda\delta)$ conformer). Since the experimental spectra were recorded in water the amino groups likely form hydrogen bonds with the solvent molecules. As we modeled solvent effects with the PCM model, explicit hydrogen bonds could not be reproduced and discrepancies for this functional group are expected. There are further experimental signals that are not matched by the present calculations. Two signals between bands ν_9 and ν_{10}, one positive and one negative, are one example. Conversely, some predicted signals are not observed in the experiment. The extent of these discrepancies might partly be resolved by including explicit solvent molecules around the complex.

This first approach in computing ROA spectra demonstrated the sensitivity of ROA towards conformations – as we got four distinctly different spectra for the four conformers. Analyzing these four conformers in detail and comparing them to the experiment allowed us to identify the conformer(s) giving the major contribution to the experimental spectrum on a visual-comparison basis. We identified the conformers $\Lambda(\delta\delta\delta)$ and $\Lambda(\lambda\delta\delta)$, with slight favor for the former, as dominant in solution; their calculated spectra show a satisfactory resemblance to the experimental one at a reasonable computational cost, since modeling the solvent effects via a simple PCM does not require huge computational effort. To analyze the effect of explicit solvent molecules the $\Lambda(\delta\delta\delta)$ conformer is further considered (see below).

In the 1970's NMR spectroscopy has been applied to the conformational analysis of *tris*(ethylenediamine)[75–78]. Beattie showed[77] that in aqueous solutions the ligands undergo an interconversion between the λ and δ conformations; in the Λ configuration, the δ conformation was predicted to be more stable than the λ conformation. But, due to statistical entropy effects, the most stable and most abundant species is expected to be $\Lambda(\lambda\delta\delta)$. However, in these studies the effect of counter ions in the conformational equilibrium was not considered; such an effect could be shown from the VCD study of $[Co(en)_3]^{3+}$[22]. The energies of the conformers obtained from the presented IEFPCM calculations are shown in Table 3. The most stable conformer, according to these values should be $\Lambda(\lambda\lambda\delta)$ (free energies); the energy differences are, however, subtle (about 1 kcal/mol $\approx$ 1.6 mHa, which is below the accuracy of the

theoretical method used). Clearly the calculated relative stabilities contradict both, the observed ROA measurements, for which the vibrational analysis was in favor of the $\Lambda(\delta\delta\delta)$ conformer, and the above mentioned NMR studies that showed, due to statistical reasons, a predominance of the $\Lambda(\lambda\delta\delta)$ conformer. The weighted spectra (a) and (b) in Figure 4 confirm the doubt raised about the reliability of the calculated weights obtained from the energies in Table 3. Furthermore, the individual spectrum (d) in the same Figure supports the vibrational analysis in favor of the $\Lambda(\delta\delta\delta)$ conformation. Spectral regions between 700 and 850 cm^{-1}, and between 1150 and 1350 cm^{-1} express this statement best. For explaining the difficulties met for the reliable determination of the energies, a potential basis set dependence can be, at least for the basis sets used, excluded; this is evidenced by the energies given as Supplementary Information (SI). These energies were obtained from calculations without use of dispersion correction or solvation model. The trend of calculated weights remain highly comparable for the three basis sets, but are not comparable to the weights obtained for the calculations with use of dispersion correction and PCM (Table 3). A thorough investigation of the causes would require highly accurate estimates of the energies of the conformers from the results of CCSD(T) calculations extrapolated to the basis set limit, for instance, followed by a careful examination of the influences of the approximations used in the DFT study. This is clearly beyond the scope of this work. Consequently, the energies listed in Table 3 will not be our choice to determine the conformer on which further investigations are conducted.

Table 3 Total energies in Hartree of the four different conformers of *tris*(ethylenediamine)rhodium(III) complex of the Λ configuration. Theoretical level: B3LYP-D/def2-TZVP (IEFPCM). E^1: SCF energies, i.e., electronic energies; E^2: Sum of electronic and thermal free energies as implemented in Gaussian 09 C.01. Weights (*w*) are calculated from Boltzmann distributions at 298K.

	$\Lambda(\lambda\lambda\lambda)$	$\Lambda(\lambda\lambda\delta)$	$\Lambda(\lambda\delta\delta)$	$\Lambda(\delta\delta\delta)$
E^1	-682.20429	-682.20428	-682.20391	-682.20338
w	32.83%	32.51%	22.06%	12.60%
E^2	-681.88629	-681.88825	-681.88715	-681.88460
w	8.58%	68.60%	21.37%	1.45%

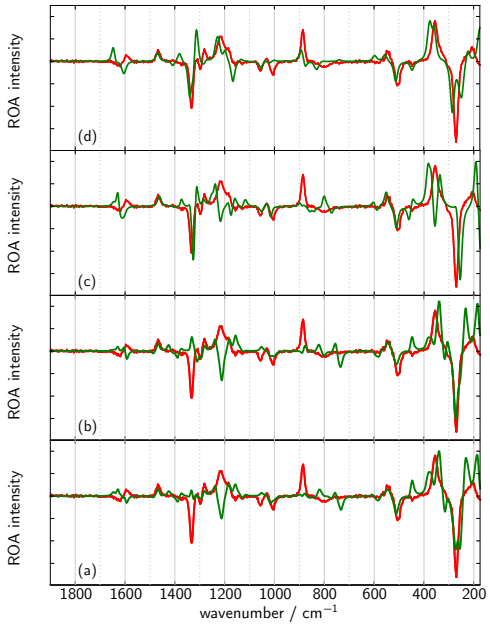

Fig. 4 Comparison of the experimental ROA spectrum (red) with theoretically predicted ones (green). (a) and (b): weighted theoretical spectra using coefficients from Table 3 for total electronic energies and the sum of electronic and thermal free energies (as implemented in Gaussian 09 C.01), respectively. Statistical abundances have been taken into account. (c) and (d): predicted spectra for the $\Lambda(\lambda\delta\delta)$ and $\Lambda(\delta\delta\delta)$ conformers, respectively. For better comparison to the experimental data, the predicted spectra were scaled with the parameters 1.028 at 545 cm^{-1} and 0.977 at 1500 cm^{-1} as implemented in PyVib2[66].

Using the resemblance between measured and predicted spectra, on the other hand, is a straightforward criterion to identify the conformer of interest. In consideration of the effort that is required to carry out a GCM analysis and a BOMD, only one conformer of the two favorable ones, namely $\Lambda(\lambda\delta\delta)$ and $\Lambda(\delta\delta\delta)$, will be selected. Without the

ability of quantifying the similarities between experimental and theoretical spectra (difficulties with respect to predicted spectra are frequency shifts, the accuracy of intensities, solvent effect, and the chosen convolution, to name a few) solely patterns are visually compared. Referring to Figure 4 (c) and (d), the $\Lambda(\delta\delta\delta)$ conformer has been chosen.

3.2.1 GCMs as a Means to Investigate the Origin of Spectral Intensities The assignment of calculated normal modes to measured bands is a key point for the comprehension of vibrational spectra. However, it keeps the scientist still in the dark about the origin of the observed intensities for recorded bands. For this, GCMs[72] can be used to shed some light onto the generation of intensities. GCMs have been defined in section 3.1 and they graphically represent contributions of reduced invariants, which have been formulated in eqs. 14–16.

The number of elements (n) in GCMs is dependent on the number of defined groups (G); since the elements are presented in upper triangular matrix form, this totals to $n = \frac{1}{2}(G + G^2)$. In order to have small GCMs, the number of groups has to remain manageable; the information withdrawn from small GCMs, in contrast, is not as detailed as for larger ones and in practice a good compromise between manageability and particularity has to be found. The choice of the distribution of atoms into groups should be done such, that the elements in the GCMs will carry a valuable information content, because it is usually of interest in which way some group of interconnected atoms contribute to the total intensity. It is then desirable to divide the molecule into groups of atoms, onto which the displacement is either significantly localized or whose positions remain barely unchanged for a given normal mode; a division into fragments that represent (the chemically more intuitive) functional groups is also in many cases a good choice. There cannot be one single definition of groups, that is best suited for all bands in a spectrum, because the particular normal modes, and thus the displacement of atoms in the molecule, are very different through the spectrum.

Table 4 provides an overview of three different choices, their identifier (G_1–G_3), the particular grouping of atoms, and the number of elements in their generated GCMs.

Table 4 Three different definitions of atom groupings for GCMs. The first column shows the identifiers (*id*), the second lists the atoms per group, followed by the one indicating the number n of resulting elements for a particular GCM. Superscripts 1–3 define the en groups. Each en group can be split in two symmetrically distinguishable parts; superscripts for the NH_2 and CH_2 groups of G_3 can carry an additional apostrophe to indicate this symmetry aspect.

id	*groups*	*n*
G_1	Rh, en^1, en^2, en^3	10
G_2	Rh, $6 \cdot NH_2$ (NH_2^{Σ}), $6 \cdot CH_2$ (CH_2^{Σ})	6
G_3	Rh, NH_2^1, CH_2^1, $CH_2^{1'}$, $NH_2^{1'}$, NH_2^2, CH_2^2, $CH_2^{2'}$, $NH_2^{2'}$, NH_2^3, CH_2^3, $CH_2^{3'}$, $NH_2^{3'}$	91

The groups G_1–G_3 are applied to analyze selected bands corresponding to the en breathing (ν_2), the *out-of-phase* en scissoring (ν_4^a, ν_4^b), the *in-phase* en scissoring (ν_5), and the CH_2 scissoring (ν_{11}^a–ν_{11}^f) vibrations. Literal superscripts are used to differentiate the normal modes belonging to the same spectral band; the sequence is strictly given in the same order as predicted by the computations (conformer $\Lambda(\delta\delta\delta)$, B3LYP-D2/def2-TZVP, IEFPCM). Figures 5 and 6 show the resulting GCMs, for G_1 and G_2, respectively, for the normal modes associated with the bands mentioned above. Due to the large number of GCM elements for G_3, Figure 7 depicts the main GCM elements only; the integral GCMs for this atom grouping are available from the supporting information (SI).

G_3 is clearly overburden with information for ν_2–ν_5 and, for these normal modes, a simpler coarse grouping of atoms is preferable; the contribution to band intensities for ν_2–ν_5 will, therefore, essentially be discussed with G_1 and G_2. On the contrary, since the normal modes of the CH_2 scissoring vibrations are highly localized on two individual CH_2 groups that can be distributed over different en bridges, the discussion for ν_{11}^a–ν_{11}^f is exclusively

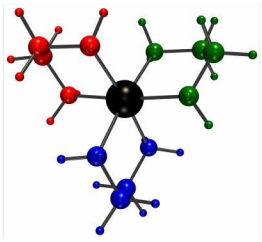

(a) atom grouping

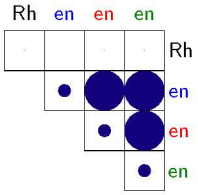

(b) ROA, sf: 1.75, en breathing (ν_2)

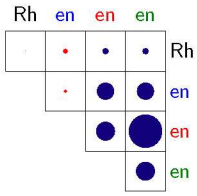

(c) ROA, sf: 0.75, *out-of-phase* en scissoring (ν_4^a)

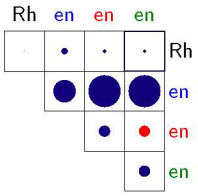

(d) ROA, sf: 0.75, *out-of-phase* en scissoring (ν_4^b)

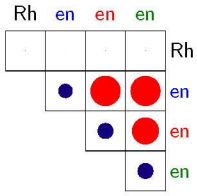

(e) ROA, sf: 0.75, *in-phase* en scissoring (ν_5)

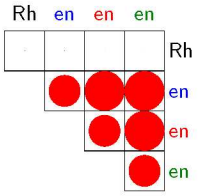

(f) Raman, sf: 2.5, *in-phase* en scissoring (ν_5)

Fig. 5 (a) shows the allocation of atoms into the defined groups, (b)–(f) show GCMs for a chosen invariant combination (ROA or Raman) and scaling factor (sf). The scaling factor allows to adapt the size of the circles best to the matrix element box. A description of the vibration is also given, followed by the identifier of the normal mode in brackets, that have been used throughout this work. For each GCM the surface area of illustrated circles is proportional to the value of the matrix element and the color indicates the sign (blue: negative, red: positive)

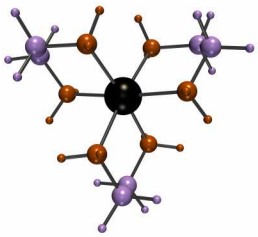

(a) atom grouping

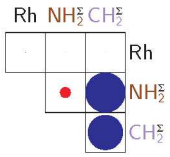

(b) ROA, sf: 3.5, en breathing (ν_2)

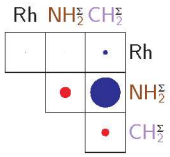

(c) ROA, sf: 2.5, *out-of-phase* en scissoring (ν_4^a)

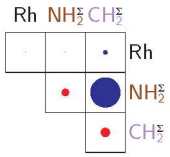

(d) ROA, sf: 2.5, *out-of-phase* en scissoring (ν_4^b)

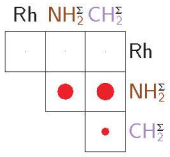

(e) ROA, sf: 2.5, *in-phase* en scissoring (ν_5)

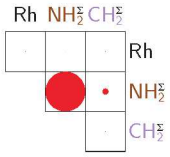

(f) Raman, sf: 12, *in-phase* en scissoring (ν_5)

Fig. 6 For details it is referred to the caption of Figure 5

carried out with G_3. As the main focus of this work is put on optical activity, GCMs are shown for ROA invariant combinations; but the remarkable *in-phase* scissoring mode in the Raman spectrum deserves to be mentioned and GCMs for the Raman invariants for this particular case are shown as well.

All GCMs share a common evidence: the contribution of the Rhodium atom by itself as well as its interaction with other groups of atoms is completely insignificant, yet zero in many cases. For this reason the following discussion is focused exclusively on parts of the ligands and aims to spot the atoms therein which are mainly responsible for the sign and size of the observed bands.

First the GCMs for G_1 in Figure 5 are reviewed.

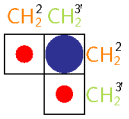

(a) ROA, sf: 0.55, *in-phase* (ν_{11}^{a})

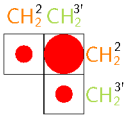

(b) ROA, sf: 0.55, *out-of-phase* (ν_{11}^{b})

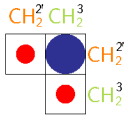

(c) ROA, sf: 0.55, *out-of-phase* (ν_{11}^{c})

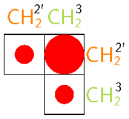

(d) ROA, sf: 0.55, *in-phase* (ν_{11}^{d})

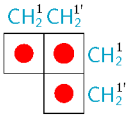

(e) ROA, sf: 0.55, *out-of-phase* (ν_{11}^{e})

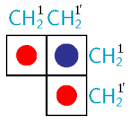

(f) ROA, sf: 0.55, *in-phase* (ν_{11}^{f})

Fig. 7 (a)–(f) show selected GCM elements (main contributions to the band intensity) for the ROA invariant combination for all normal modes of the CH_2 scissoring vibration ν_{11}. Normal modes are distinguished by the superscripts *a–f*. For further information with respect to the CH_2 group identifiers, i.e., 1–3', the reader is referred to the caption of Table 5, where these are explained in detail. The groups of atoms are indicated in Table 4, therein called G_3. For each GCM the surface area of illustrated circles is proportional to the value of the matrix element and the color indicates the sign (blue: negative, red: positive). The GCMs for all elements of these normal modes are available from the supporting information (SI)

The three en groups are symmetry equivalent in the $\Lambda(\delta\delta\delta)$ conformation. For totally symmetric normal modes a symmetric pattern in the corresponding GCM is expected. The GCMs for ν_2 and ν_5 confirm this statement. It can be seen for ν_2, that the great majority of the negative intensity is produced by the interaction terms between the three en bridges. Small negative contributions are added from each individual en bridge. Similar intra-group contributions are observed in ν_5, but, in contrast, the interaction between the bridges causes positive intensity shares. The resulting, overall positive band intensity for ν_5 is thus smaller than for ν_2, due to partial compensation by the negative en intra-group contributions and due to the overall smaller values of the represented inter-group quantities. ν_4^a and ν_4^b have lower symmetry and, therefore, a non-symmetric pattern is anticipated. The predominant contributions for the observed negative intensities of these two bands stem from the interaction between en bridges. It is, however, difficult to make an accurate statement about the nature of the interactions.

Even though G_2 is coarser it tells somewhat more precisely about the origin of the intensities for ν_4^a and ν_4^b: they are evidently generated by the interaction of the NH_2 and CH_2 groups – even if G_2 is blind to differentiate between contributions generated on one en bridge or when two bridges might be involved. An additional information is also accounted for ν_2: CH_2 groups contribute almost as much to the total intensity as the interaction between CH_2 and NH_2 groups. As for the previous case, G_2 gives a valuable insight, but is for some normal modes not detailed though. If knowledge about the nature of the interactions is desired, a grouping such as G_3 should be used; this comes with the price of a laborious evaluation.

The CH_2 scissoring normal modes ν_{11}^a–ν_{11}^f are analyzed with G_3, as stated above. The 6 vibrations can be split into 3 pairs (P_1–P_3) of an *in-phase* and *out-of-phase* combination for two involved CH_2 fragments, respectively. Table 5 provides details about the localization of the vibration in the complex and defines P_1–P_3. The GCMs comprising major elements responsible for observed intensities are placed in Figure 7 (all emenent are available in the supplementary information (SI)). The two GCMs for each pair P_1, P_2, and P_3 exhibit a common behavior: intra-group contributions of the fragments where the vibration is localized are small but always positive; the inter-group contributions for these fragments are of opposite sign in the two concerned GCMs – and thus cancel each other out; other GCM terms are often zero, sometimes minor, and roughly add up to zero as well. The observed weak and broad positive band of the CH_2 scissoring mode vibrations is solely the result from rather small intra-CH_2-group contributions which do not cancel out for a *in-phase/out-of-phase* combination.

Table 5 *top*: pictorial illustration of all defined groups in G_3. *bottom*: CH_2 scissoring modes ν_{11}^a–ν_{11}^f. 3 groups of pairs (P) for *in-phase* and *out-of-phase* combinations located on the same CH_2 fragments, respectively, are listed. Superscripts for CH_2 groups indicate on which en group they are located (number) and on which side of the en bridge they are (potential apostrophe)

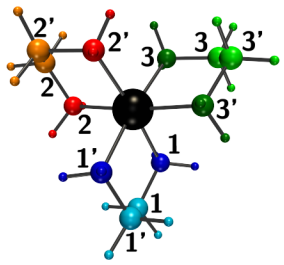

pair	*id*	*fragments*	*phase relation*
P_1	ν_{11}^a	CH_2^2, $CH_2^{3'}$	*in-phase*
	ν_{11}^b	CH_2^2, $CH_2^{3'}$	*out-of-phase*
P_2	ν_{11}^c	$CH_2^{2'}$, CH_2^3	*out-of-phase*
	ν_{11}^d	$CH_2^{2'}$, CH_2^3	*in-phase*
P_3	ν_{11}^e	CH_2^1, $CH_2^{1'}$	*out-of-phase*
	ν_{11}^f	CH_2^1, $CH_2^{1'}$	*in-phase*

Before concluding this section, the Raman GCMs for ν_5 are surveyed. The Raman GCM for G_2 tells us, that the strong positive band is utterly due to interactions between NH_2 fragments of the complex. It can be seen from the G_1 Raman GCM, that these NH_2 interactions occur within individual en bridges, but that strong interactions between different en ligands are present.

For selected bands and their attributed normal modes the corresponding GCMs gave a profound insight into the generation of observed intensities. When a meaningful choice for the groups of atoms was made, the GCMs provided valuable information about the interaction between fragments of the Rh complex. In some cases the combined information from different grouping choices was necessary to improve the conclusions drawn. The information gained from this type of analysis enhances the understanding of vibrational spectra.

3.2.2 Influence of Hydrogen Bonds Earlier studies on solvation effects in ROA calculations[26,37,39,79,80] showed that, for protic solvents, taking explicitly some solvent molecules into account – usually first hydration sphere is sufficient – results in a better description of the spectrum as compared to the results achieved using a continuum solvation model. Jalkanen *et al.*[37] showed that a complete encapsulation of the molecule with solvent molecules and the use of continuum solvation models for bulk solvent yields good results.

Therefore, in order to deepen our understanding of the role of the solvent and especially of the influence of the solute-solvent H-bond interactions on the ROA properties of $[Rh(en)_3]^{3+}$, a BOMD simulation has been performed at 300 K on the $\Lambda(\delta\delta\delta)$ conformer in order to characterize its aqueous solution structure and the organization of its solvation shell. Figure 8 shows a snaphsot taken from the trajectory. It illustratres the H-bonding network and the involvement of the NH_2 groups of the ligands.

The structure of $\Lambda(\delta\delta\delta)$-$[Rh(en)_3]^{3+}$ in solution has been characterized by calculating the thermal distributions of the average Rh—N bond length, of the average values of the bite angle $\beta = \angle$N—Rh—N, and of the dihedral angle $\gamma = \angle$N—C—C—N. They are drawn in Figure 9. Inspection of this figure shows that the distributions could satisfactorily be fitted with Gaussian distribution functions. From the averages and standard deviations obtained from the fit, we have for $\Lambda(\delta\delta\delta)$-$[Rh(en)_3]^{3+}$: r(Rh—N) = 2.106 ± 0.048 Å; $\beta = 82.7 \pm 2.2$ deg; and $\gamma = 52.3 \pm 6.3$ deg. These values are in good agreement with those found in the optimized geometry of the conformer (Table 2).

The average structure of $\Lambda(\delta\delta\delta)$-$[Rh(en)_3]^{3+}$ in water has also been calculated, along with the root-mean-square fluctuations of the atomic positions about their average values. The average structure is shown in Figure 10 with the 50% probability ellipsoids associated with the thermal fluctuations of the atoms. There is an increase of the volumes of the ellipsoids, hence of the atomic disorders, on moving away from the Rh atom. For the hydrogen atoms, as

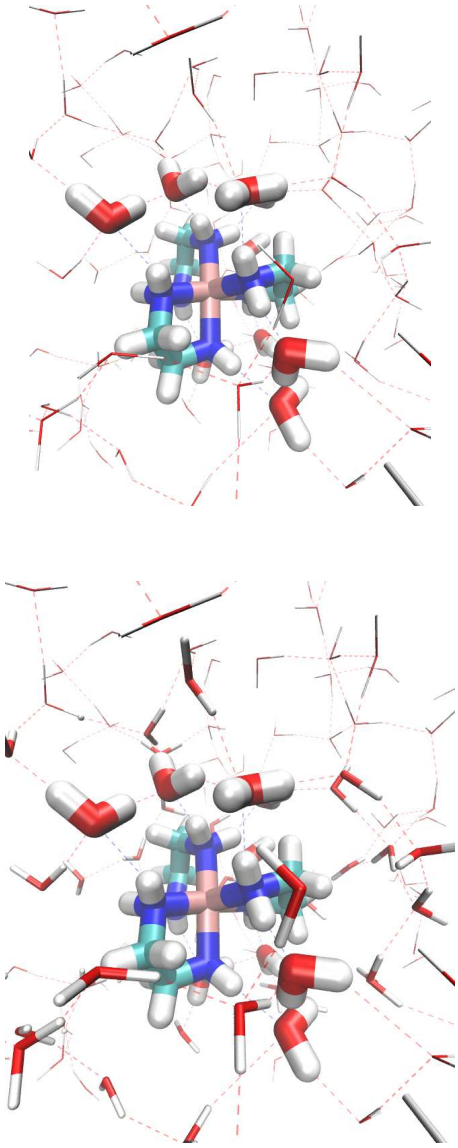

Fig. 8 BOMD study of $\Lambda(\delta\delta\delta)$-$[Rh(en)_3]^{3+}$: snapshot from the trajectory showing the complex, some water molecules, and the H-bonding network. *top:* The water molecules in the first solvation shell of the complex are drawn using a large bond radius for the licorice representation while a line representation is adopted for the other water molecules. *bottom:* The water molecules in the second solvation shell of the complex are emphasized by drawing them using a licorice representation with an intermediate bond radius

compared to the carbon or nitrogen atoms, this disorder seems to be stronger than expected when considering merely the longer distance from the center atom. This increase of the thermal fluctuations follows from their increased exposure to the solvent.

In order to characterize the organization of the solvent around $\Lambda(\delta\delta\delta)$-$[Rh(en)_3]^{3+}$, the radial distribution functions (RDFs) $g(r)$ of the water oxygen (O_w) and hydrogen (H_w) with respect to the Rh atom have been calculated using a 0.1 Å radial grid. The RDFs are plotted in Figure 11 with the associated running coordination numbers $cn(r)$. The comparison in Figure 11 of the Rh−O_w and Rh−H_w RDFs and running coordination numbers shows that the water oxygen atoms can get closer to the Rh atom than the water hydrogen atoms. This preferred orientation of the water molecules in the vicinity of $[Rh(en)_3]^{3+}$ is explained by the large positive charge of the complex and the involvement of the oxygen atoms in NH···O hydrogen bonds (Figure 8). The Rh−O_w RDF presents a broad peak with a maximum at ∼4.2 Å and a minimum at ∼5.1 Å, which defines the first solvation shell. It also presents a second broad peak centered at ∼6.2 Å, which defines the second solvation shell.

Before going further into the analysis of the BOMD simulation results, let us again stress upon the fact that this simulation study is by no means intended to be an exhaustive account of the compared performances of implicit versus explicit solvation modeling of ROA spectra, as has been reported for lactamide and 2-aminopropanol by Hopmann *et al.* [26]. For such a performance assessment, several hundreds of snapshots should be considered[26]. However, considering that no conformational change occurred during the simulation and that the signs of the ROA main features remained the same for all the snapshots, we believe that the present analysis of the BOMD simulation results allows us to gain valuable insights into the influence of the first solvation shell on the ROA spectrum of the complex.

There are ∼9 water molecules in the first solvation shell, which has explicitly been taken into account in subsequent ROA calculations on aqueous $\Lambda(\delta\delta\delta)$-$[Rh(en)_3]^{3+}$. To assess the influence

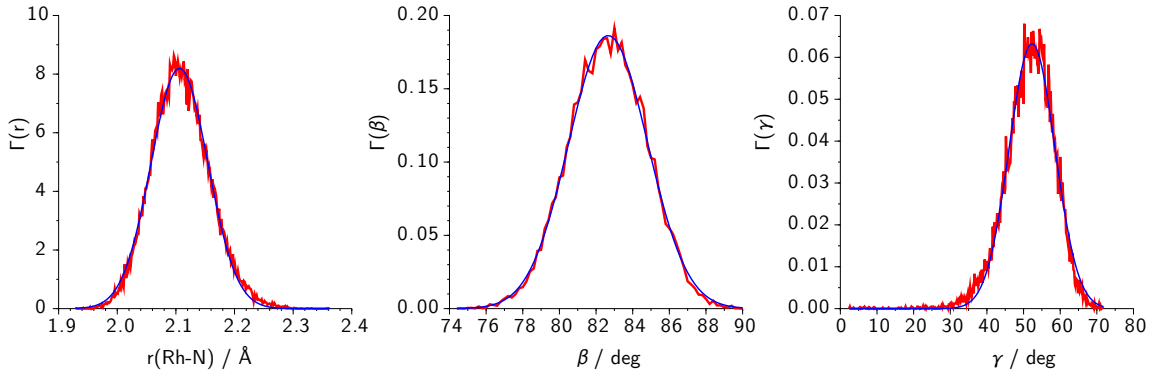

Fig. 9 Thermal distributions of the average Rh−N, β, and γ structural parameters (red lines) in aqueous $\Lambda(\delta\delta\delta)$-$[Rh(en)_3]^{3+}$. The results of their fits to Gaussian distributions are also shown (blue lines)

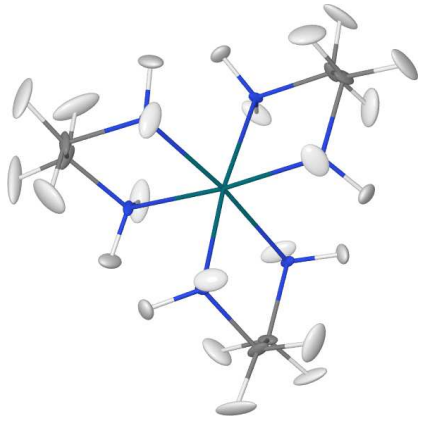

Fig. 10 View of the average structure of aqueous $\Lambda(\delta\delta\delta)$-$[Rh(en)_3]^{3+}$ with 50% probability ellipsoids

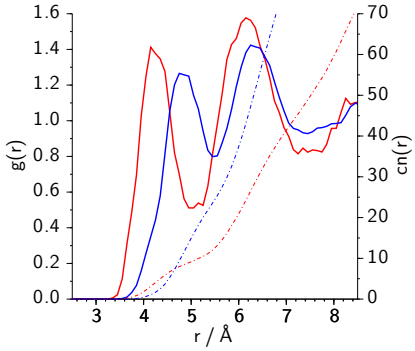

Fig. 11 Organization of the solvent around $\Lambda(\delta\delta\delta)$-$[Rh(en)_3]^{3+}$: Rh−$O_w$ (red lines) and Rh−H_w (blue lines) radial distribution functions (solid lines, left *y*-axis) and running coordination numbers (dot-dashed lines, right *y*-axis)

of H-bonding on the ROA spectra of $\Lambda(\delta\delta\delta)$-$[Rh(en)_3]^{3+}$ in aqueous solution, the ROA spectra were calculated on conformer-water clusters obtained from 14 snapshots taken every 2.5 ps, and consisting of the conformer and the 9 closest water molecules. The solvation effects due to the outer solvation shells and the bulk remained modeled by the polarizable continuum model. A detailed analysis in terms of GCMs, as discussed in the previous subsection, would be desirable but too extensive. The GCMs for each snapshot for a given normal mode are different due to the variable influence of the water molecules beside the fact that more normal modes have to be considered. Furthermore, the atomic excursions are affected by the water shell and cannot directly be mapped to the ones of the naked $\Lambda(\delta\delta\delta)$-$[Rh(en)_3]^{3+}$ structure without solvation sphere. Therefore only one example for the snapshot around the half time of the BOMD simulation, at 15 ps, and for the en breathing mode, designated ν_2 in Figure 2 and Table 1, is presented.

The normal mode, whose atomic excursions refer to the en breathing mode ν_2 calculated at 274 cm^{-1}, is easily identified in the $\Lambda(\delta\delta\delta)$-$[Rh(en)_3]^{3+}$ conformer without solvation sphere (designated as ref-

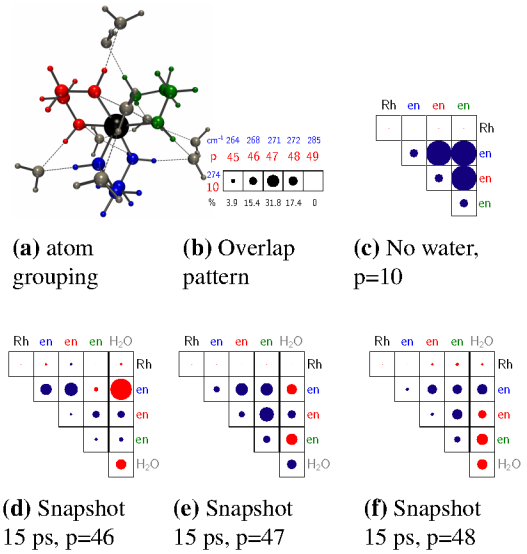

(a) atom grouping **(b)** Overlap pattern **(c)** No water, p=10

(d) Snapshot 15 ps, p=46 **(e)** Snapshot 15 ps, p=47 **(f)** Snapshot 15 ps, p=48

Fig. 12 (a) shows the allocation of atoms into defined groups, (b) is the overlap pattern of normal mode 10 of $\Lambda(\delta\delta\delta)$-$[Rh(en)_3]^{3+}$ with the Rhodium complex in the snapshot. (c)–(f) depict ROA GCMs for ν_2, i.e., the en breathing mode, scaling factor: 1.75. The overlap pattern helps to identify which normal modes p of the snapshot calculation match best the reference en breathing mode (p=10) of the $\Lambda(\delta\delta\delta)$-$[Rh(en)_3]^{3+}$ calculation without explicit water molecules. A thicker line separates the GCMs in (d)–(f); left parts can be compared to (c), the right parts reflect the interaction of the water molecules with groups defined in the Rhodium complex and the contribution of the solvation shell

erence calculation hereafter). The overlaps of the nuclear motions for the atoms in the Rhodium complex in the reference calculation with the nuclear motions in a trial calculation can be obtained[81]; these overlaps contain information on how much individual normal modes of the trial calculation match the nuclear excursions of the reference normal mode in form and intensity. Figure 12 (b) shows the relevant part of the overlap matrix with respect to the en breathing mode. The overlap pattern shows three normal modes in the snapshot that have contributions higher than 10%, i.e., normal mode numbers 46, 47, and 48 with overlaps of 15.4%, 31.8%, and 17.4% at 268 cm^{-1}, 271 cm^{-1}, and 272 cm^{-1}, respectively. Figure 12 (c) shows the reference GCM (copy of Figure 5 (b)) and serves as comparison for the three GCMs for the considered normal modes of the snapshot (Figure 12 (d)–(f)). Figure 12 (a) depicts the definition of groups used to create these GCMs. When compared to the reference GCM (c), the pattern in GCMs (e) and (f) are similar. The negative contributions from the complex stem mainly from en interactions and to a smaller extent from the en groups themselves; the Rhodium is uninvolved. The interaction of the solvation sphere with the complex is not negligible and leads to an overall (small) positive contribution to the signal. The influence of water for the snapshot normal mode 46, (d), is most pronounced: the interaction with the first en group, illustrated in blue, is dominant and positive.

With help of GCMs the influence of the solvation sphere to the observed intensities can be studied. In principle the molecules of the solvation sphere themselves could be split into several groups which would lead to a more profound understanding. But, as mentioned above, the number of snapshots and normal modes to consider is too large and such a detailed analysis is beyond the scope of this work. Therefore the results of the BOMD snapshots are qualitatively discussed below.

The mean Raman and ROA spectra shown in Figure 13 (b) were actually calculated after structure optimization of the clusters extracted from the considered snapshots obtained from the BOMD simulation. The mean spectra of the snapshots show an overall improved agreement with experiment; even though some negative bands are overemphasized, i.e., at 870 cm^{-1} (NH_2 and CH_2 rocking, partially coupled with C-C stretching) and 1190 cm^{-1} (NH_2 and CH_2 twisting and wagging). Other pattern, i.e., around 1330 cm^{-1} and 1700 cm^{-1} (NH_2 scissoring), emerge from the mixture of shapshots to a much better resemblance with the experiment as compared to the spectra of the four previously discussed conformers without explicit solvent molecules. With respect to the whole set of selected vibrational bands listed in Table 1, they can roughly be categorized into three different cases: (*i*)

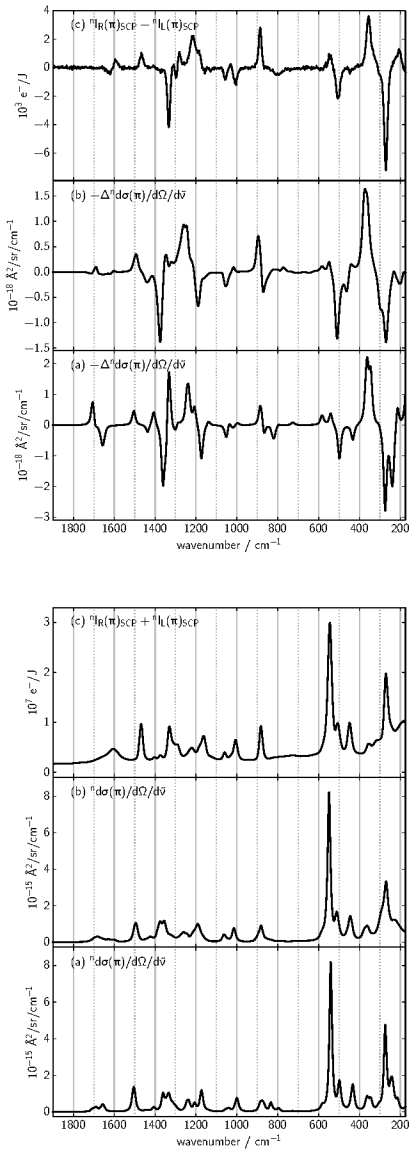

Fig. 13 ROA (*top*) and Raman (*bottom*) spectra – comparison of the theoretical spectrum of the $\Lambda(\delta\delta\delta)$–$[Rh(en)_3]^{3+}$ conformer (a), the average spectrum obtained from the 14 AIMD snapshots with first solvation sphere (b), and the experimental spectrum (c). One snapshot each 2.5 ps was taken till 32.5 ps; all theoretical spectra for (b) were weighted equally

the band intensities are rather unaffected by the explicit presence of water molecules and correspond to experimental observations (ν_3–ν_6 and ν_9–ν_{11}), (*ii*) those bands whose intensities remain inaccurately predicted (ν_7 and ν_8), (*iii*) and bands that strongly change from snapshot to snapshot (ν_1, ν_2, ν_{12}, and ν_{13}). For the latter case snapshots at 22.5 ps and 30.0 ps, available as Supporting Information (SI), are mentioned, where the NH_2 scissoring vibrations (ν_{12} and ν_{13}) agree with the measured spectrum.

The sign sequence of characteristic band intensity patterns, that might be used for the determination of the absolute configuration of the complex, does not drastically change throughout the considered snapshots.

4 Conclusions

Δ- and Λ-*tris*-(ethylenediamine)rhodium(III) have been synthesized and their backward scattering Raman and ROA spectra measured in aqueous solution. The Raman spectra show no notable background.

Computations were used to investigate the spectra. The combination of the B3LYP-D2 functional with the def2-TZVP basis set within the IEFPCM model was chosen to predict the vibrational spectra. The comparison between the spectra of the four possible conformations with experiment encouraged to use the $\Lambda(\delta\delta\delta)$-$[Rh(en)_3]^{3+}$ conformation for further investigations of the origin of observed intensities and of solvation effects. The two most stable conformers according to the calculations are not compatible with the measured ROA spectra.

Applying a GCM analysis to selected predominant bands showed that the Rhodium atom does not contribute to the observed intensities. The band associated to the en breathing mode arises mainly from the interaction between the three en ligands, whereas the intensity of the *out-of-phase* en scissoring band is essentially due to contributions of interactions between the NH_2 and CH_2 groups.

The influence of solvent molecules has been examined by performing a BOMD simulation. Radial distribution functions for the water oxygen and hy-

drogen atoms showed that the water molecules are oriented with the oxygen atoms pointing towards the Rhodium complex; the first two solvation shells are at a distance of ∼4.2 and ∼6.2 Å from the Rh atom. 14 snapshots have been taken, and their spectra of the Rhodium complex with first solvation sphere calculated after re-optimization within the IEFPCM model; the mean of these spectra is in much better agreement with the experiment. For one snapshot, and the en breathing mode, the influence of the first solvation sphere was inspected by means of GCMs. The water molecules interact strongly with the complex and contribute to the band intensities, which shows that explicit solvent molecules have to be taken into account for accurate predictions.

5 Acknowledgements

Financial support from the Swiss National Science Foundation and the University of Geneva is acknowledged. We thank Prof. W. Hug for his support. This work was supported by a grant from the Swiss National Supercomputing Centre (CSCS) under projects ID s103 and s501, and by a grant from the Center for Advanced Modeling Science(CADMOS) under project ID CTESIM. The financial support for CADMOS and for the BlueGene/Q system is provided by Geneva Canton, Vaud Canton, fondation of Hans Wilsdorf, fondation of Louis-Jeantet, the University of Geneva, the University of Lausanne, and the Ecole Polytechnique Fédérale de Lausanne.

6 ESI

Comparison of ROA spectra for the $\Lambda(\lambda\lambda\lambda)$ conformer using the TZVP basis set (CEP-121G for Rh) in conjunction with the B3LYP, B3LYP-D, and B3LYP-D+IEFPCM; comparison of ROA spectra for the $\Lambda(\lambda\lambda\lambda)$ conformer utilizing the B3LYP-D density functional in combination with the basis sets TZVP(C,N,H)/CEP-121G(Rh), def2-TZVP, and def2-TZVPD; experimental and theoretical geometry parameters for the four conformers ($\Lambda(\lambda\lambda\lambda)$, $\Lambda(\lambda\lambda\delta)$, $\Lambda(\lambda\delta\delta)$, and $\Lambda(\delta\delta\delta)$); tabulated ROA band positions and signs; individual Raman, ROA, and degree of circularity spectra for the four previously mentioned conformers (level of theory: B3LYP-D/def2-TZVP/IEFPCM); extensive GCMs for atom grouping G_3 (see Table 4) and all normal modes considered in section 3.2.1; summary of the synthesis and enantioseparation described by Galsbøl [28]; tabulated characteristic structural parameters for the 14 optimized $\Lambda(\delta\delta\delta)$ snapshots obtained during the BOMD run; comparison of the average spectrum of the 14 snapshots to the experimental spectra; individual Raman and ROA spectra of the 14 optimized $\Lambda(\delta\delta\delta)$ snapshots; comparative spectra B3LYP/def2-TZVP of the $\Lambda(\lambda\lambda\delta)$ conformer obtained with Gaussian 09 revisions C01 and D01; Total energies and weights for the four conformers and the TZVP, def2-TZVP, and def2-TZVPD basis sets combined with the B3LYP functional.

References

1 L. A. Nafie, G. S. Yu, X. Qu and T. B. Freedman, *Faraday discussions*, 1994, 13–34; discussion 87–101.
2 L. D. Barron and A. D. Buckingham, *Chem. Phys. Lett.*, 2010, **492**, 199.
3 Y. He, B. Wang, R. K. Dukor and L. a. Nafie, *Applied spectroscopy*, 2011, **65**, 699–723.
4 L. A. Nafie, *Vibrational Optical Activity*, John Wiley & Sons, Ltd, Chichester, UK, 2011.
5 L. Barron, M. P. Bogaard and A. D. Buckingham, *Journal of the American Chemical Society*, 1972, **95**, 603–605.
6 L. Barron, M. Bogaard and A. Buckingham, *Nature*, 1973, **241**, 113–114.
7 L. D. Barron and A. D. Buckingham, *J.C.S. Chem. Comm.*, 1973, 152–153.
8 W. Hug, S. Kint, G. F. Bailey and J. R. Scherer, *Journal of the American Chemical Society*, 1975, **97**, 5589–5590.
9 K. M. Spencer, T. B. Freedman and L. A. Nafie, *Chemical Physics Letters*, 1988, **149**, 367 – 374.
10 L. Hecht and L. D. Barron, *Faraday Discussions*, 1994, **99**, 35.
11 W. Hug and G. Hangartner, *J. Raman Spectrosc.*, 1999, **30**, 841–852.
12 J. Haesler and W. Hug, *CHIMIA International Journal for Chemistry*, 2008, **62**, 482–488.
13 J. Kapitán, V. Baumruk and P. Bour, *Journal of the American Chemical Society*, 2006, **128**, 2438–43.
14 F. Zhu, P. Davies, A. R. Thompsett, S. M. Kelly, G. E. Tran-

ter, L. Hecht, N. W. Isaacs, D. R. Brown and L. D. Barron, *Biochemistry*, 2008, **47**, 2510–7.
15 L. D. Barron, L. Hecht, I. H. McColl and E. W. Blanch, *Molecular Physics*, 2004, **102**, 731–744.
16 A. Synytsya, M. Judexová, T. Hrubý, M. Tatarkovič, M. Miškovičová, L. Petruželka and V. Setnička, *Analytical and bioanalytical chemistry*, 2013, **405**, 5441–53.
17 C. Merten, H. Li, X. Lu and L. A. Nafie, *J. Raman Spectrosc.*, 2010, **2010**, 1563–1565.
18 C. Johannessen, L. Hecht and C. Merten, *Chemphyschem : a European journal of chemical physics and physical chemistry*, 2011, **12**, 1419–21.
19 S. Luber and M. Reiher, *Chemical Physics*, 2008, **346**, 212–223.
20 S. Luber and M. Reiher, *Chem. Phys. Chem.*, 2010, **11**, 1876.
21 M. R. Oboodi, B. B. Lal, D. A. Young, T. B. Freedman and L. A. Nafie, *Journal of the American Chemical Society*, 1985, **107**, 1547–1556.
22 D. A. Young, T. B. Freedman, E. D. Lipp and L. A. Nafie, *J. Am. Chem. Soc.*, 1986, **108**, 7255–7263.
23 T. B. Freedman, X. Cao, D. A. Young and L. A. Nafie, *The Journal of Physical Chemistry A*, 2002, **106**, 3560–3565.
24 A. H. Pandith and S. K. Pati, *The journal of physical chemistry. A*, 2010, **114**, 87–92.
25 M. Pecul, E. Lamparska, C. Cappelli, L. Frediani and K. Ruud, *J. Phys. Chem. A*, 2006, **110**, 2807.
26 K. H. Hopmann, K. Ruud, M. Pecul, A. Kudelski, M. Dracinsky and P. Bour, *J. Phys. Chem. B*, 2011, **115**, 4128.
27 *Nomenclature of Inorganic Chemistry, IUPAC recommendations 2005*, ed. N. G. Connelly, T. Damhus, R. M. Hartshorn and A. T. Hutton, RSCPublishing, Norfolk UK, 2005, p. 366.
28 F. Galsbøl, *Inorganic Sytheses*, 1970, **12**, 269–280.
29 W. Hug, in *Comprehensive Chiroptical Spectroscopy*, ed. N. Berova, P. L. Polavarapu, K. Nakanishi and R. W. Woody, 2012, vol. 1, pp. 147–177.
30 J. Haesler, *Ph.D. thesis*, Department of Chemistry, University of Fribourg (CH), 2006.
31 W. Hug, *Applied Spectroscopy*, 2003, **57**, 1–13.
32 P. Hohenberg and W. Kohn, *Phys. Rev.*, 1964, **136**, B864–B871.
33 W. Kohn and L. J. Sham, *Phys. Rev.*, 1965, **140**, A1133–A1138.
34 A. D. Becke, *J. Chem. Phys.*, 1993, **98**, 5648.
35 C. Lee, W. Yang and R. G. Parr, *Phys. Rev. B*, 1988, **37**, 785.
36 B. Miehlich, A. Savin, H. Stoll and H. Preuss, *Chem. Phys. Lett.*, 1989, **157**, 200.
37 K. J. Jalkanen, I. M. Degtyarenko, R. M. Nieminen, K. Cao, L. A. Nafie, F. Zhu and L. D. Barron, *Theor Chem Account*, 2008, **119**, 191.
38 J. Sebestik and P. Bour, *J. Phys. Chem. Lett.*, 2011, **2**, 498.
39 M. Kaminski, A. Kudelski and M. Pecul, *J. Phys. Chem. B*, 2012, **116**, 4976.
40 X. Li, K. H. Hopmann, J. Hudecova, W. Stensen, J. Novotna, M. Urbanova, J.-S. Svendsen, P. Bour and K. Ruud, *J. Phys. Chem. A*, 2012, **116**, 2554.
41 J. Tomasi, B. Mennucci and R. Cammi, *Chem. Rev.*, 2005, **105**, 2999.
42 M. J. Frisch, G. W. Trucks, H. B. Schlegel, G. E. Scuseria, M. A. Robb, J. R. Cheeseman, G. Scalmani, V. Barone, B. Mennucci, G. A. Petersson, H. Nakatsuji, M. Caricato, X. Li, H. P. Hratchian, A. F. Izmaylov, J. Bloino, G. Zheng, J. L. Sonnenberg, M. Hada, M. Ehara, K. Toyota, R. Fukuda, J. Hasegawa, M. Ishida, T. Nakajima, Y. Honda, O. Kitao, H. Nakai, T. Vreven, J. A. Montgomery, Jr., J. E. Peralta, F. Ogliaro, M. Bearpark, J. J. Heyd, E. Brothers, K. N. Kudin, V. N. Staroverov, R. Kobayashi, J. Normand, K. Raghavachari, A. Rendell, J. C. Burant, S. S. Iyengar, J. Tomasi, M. Cossi, N. Rega, J. M. Millam, M. Klene, J. E. Knox, J. B. Cross, V. Bakken, C. Adamo, J. Jaramillo, R. Gomperts, R. E. Stratmann, O. Yazyev, A. J. Austin, R. Cammi, C. Pomelli, J. W. Ochterski, R. L. Martin, K. Morokuma, V. G. Zakrzewski, G. A. Voth, P. Salvador, J. J. Dannenberg, S. Dapprich, A. D. Daniels, . Farkas, J. B. Foresman, J. V. Ortiz, J. Cioslowski and D. J. Fox, *Gaussian 09*, Gaussian Inc. Wallingford CT 2009.
43 V. Liégeois, K. Ruud and B. Champagne, *The Journal of chemical physics*, 2007, **127**, 204105.
44 K. Ruud, T. Helgaker and P. Bour, *J.*, 2002, 7448–7455.
45 M. Pecul and K. Ruud, *Int. J. Quan. Chem.*, 2005, **104**, 816.
46 K. Ruud and A. J. Thorvaldsen, *Chirality*, 2009, **21**, E54.
47 A. Schäfer, C. Huber and R. Ahlrichs, *J. Chem. Phys.*, 1994, **100**, 5829–5835.
48 W. J. Stevens, M. Krauss, H. Basch and P. G. Jasien, *Can. J. Chem.*, 1992, **70**, 612–630.
49 F. Weigend and R. Ahlrichs, *Phys. Chem. Chem. Phys.*, 2005, **7**, 3297–3305.
50 D. Andrae, U. Häußermann, M. Dolg, H. Stoll and H. Preuß, *Theor. Chim. Acta*, 1990, **77**, 123–141.
51 D. Rappoport and F. Furche, *J. Chem. Phys.*, 2010, **133**, 134105.
52 C. van Wüllen, *The Journal of chemical physics*, 2012, **136**, 114110.
53 B. Hess, C. Kutzner, D. van der Spoel and E. Lindahl, *J. Chem. Theory. Comput.*, 2008, **4**, 435–447.
54 C. Caleman, P. J. van Maaren, M. Hong, J. S. Hub, L. T. Costa and D. van der Spoel, *J. Chem. Theory Comput.*, 2012, **8**, 61–74.
55 S. Grimme, J. Antony, S. Ehrlich and H. Krieg, *J. Chem. Phys.*, 2010, **132**, 154104.
56 J. VandeVondele, M. Krack, F. Mohamed, M. Parrinello, T. Chassaing and J. Hutter, *Comp. Phys. Comm.*, 2005, **167**, 103–128.
57 S. Goedecker, M. Teter and J. Hutter, *Phys. Rev. B*, 1996, **54**, 1703–1710.
58 C. Hartwigsen, S. Goedecker and J. Hutter, *Phys. Rev. B*, 1998, **58**, 3641–3662.
59 M. Krack, *Theor. Chem. Acc.*, 2005, **114**, 145–152.
60 J. VandeVondele and J. Hutter, *J. Chem. Phys.*, 2007, **127**, 114105.
61 G. J. Martyna, M. L. Klein and M. Tuckerman, *J. Chem.*

Phys., 1992, **97**, 2635–2643.
62 W. Humphrey, A. Dalke and K. Schulten, *J. Mol. Graphics*, 1996, **14**, 33–38.
63 J. Stone, *M.Sc. thesis*, Computer Science Department, University of Missouri-Rolla, 1998.
64 *"Jmol: an open-source Java viewer for chemical structures in 3D"*, http://www.jmol.org (accessed Feb. 26, 2014).
65 B. McMahon and R. M. Hanson, *J. Appl. Cryst.*, 2008, **41**, 811–814.
66 M. Fedorovsky, *PyVib2, a program for analyzing vibrational motion and vibrational spectra*, http://pyvib2.sourceforge.net, 2007.
67 P. W. Atkins and L. D. Barron, *Molecular Physics*, 1969, **16**, 453–466.
68 L. Barron and A. D. Buckingham, *Molecular Physics*, 1971, **20**, 1111–1119.
69 L. Hecht and L. A. Nafie, *Molecular Physics*, 1991, **72**, 441–469.
70 L. D. Barron, *Molecular Light Scattering and Optical Activity*, Cambridge University Press, 2004.
71 W. Hug, in *Continuum Solvation Models in Chemical Physics: From Theory to Applications*, ed. B. Mennucci and R. Cammi, 2007, ch. 2.6, Raman Optical Activity, pp. 221–237.
72 W. Hug, *Chemical Physics*, 2001, **264**, 53–69.
73 A. D. Buckingham, *Adv. Chem. Phys.*, 1967, **12**, 107–142.
74 A. Whuler, C. Brouty, P. Spinat and P. Herpin, *Acta Cryst.*, 1976, **B32**, 2238.
75 J. R. Gollogly and C. J. Hawkins, *Inorg. Chem.*, 1970, **9**, 576.
76 J. R. Gollogly, C. J. Hawkins and J. K. Beattie, *Inorg. Chem.*, 1971, **10**, 317.
77 J. K. Beattie, *Accounts of Chemical Research*, 1971, **4**, 253.
78 J. L. Sudmeier and G. L. Blackmer, *Inorg. Chem.*, 1971, **10**, 2010.
79 S. Luber and M. Reiher, *The journal of physical chemistry. A*, 2009, **113**, 8268–77.
80 J. R. Cheeseman, M. S. Shaik, P. L. a. Popelier and E. W. Blanch, *Journal of the American Chemical Society*, 2011, **133**, 4991–7.
81 W. Hug and M. Fedorovsky, *Theoretical Chemistry Accounts*, 2006, **119**, 113–131.